ARTICLE OPEN

Check for updates

Intrinsically flexible all-carbon-nanotube electronics enabled by a hybrid organic–inorganic gate dielectric

Qiuyue Huang[1,3], Jialiang Wang[2,3], Chenglin Li[1], Jiahao Zhu[1,2], Wanting Wang[1], Youchao Huang[1], Yiming Zhang[1], Hailong Jiao[1], Shengdong Zhang[1], Hong Meng[2], Min Zhang[1]✉ and Xinwei Wang[2]✉

The advancement of Internet of Things has stimulated huge demands on low-voltage flexible electronics. Carbon-nanotube (CNT)-based electronics are of great promise to this end for their intrinsic flexibility, high carrier mobility, and capability to synthesize as semiconducting or metallic to serve as the channels, electrodes, and interconnects of circuits. However, the gate dielectric often has to adopt brittle oxides, which can seriously limit the device flexibility. Herein, we show that a hybrid polyimide-Al_2O_3 material can serve as a good gate dielectric to realize truly intrinsic flexibility of transistors and circuits based on CNTs. With this hybrid dielectric, high-performance all-CNT transistors and integrated circuits of inverters, ring oscillators, and logic gates are demonstrated. Particularly, the inverters exhibit a remarkably high gain of 342.5 and can be used as an analog amplifier for millivolt small signals. Ultralow voltage (50 mV) operation is also feasible, which highlights the great promise for low-power applications.

npj Flexible Electronics (2022)6:61 ; https://doi.org/10.1038/s41528-022-00190-8

INTRODUCTION

The Internet of Things (IoT) and artificial intelligence has significantly facilitated our way of living by introducing many emerging 'smart' technologies, such as smart robots, smart home, smart city, and smart industries. Flexible wearable electronics constitute the key building blocks in these smart technologies, which closely connect the human body to the electronics nearby as well as over the world. Many cutting-edge areas, such as medicine and healthcare[1,2], perception and intelligent robots[3], and brain-machine interfaces[4], have intensively adopted the flexible electronics technology to dramatically expand their functionalities. In contrast to traditional microelectronics, flexible electronics are mainly built on thin-film transistors (TFTs)[5], which serve as the indispensable integrable elements for flexible analog and digital integrated circuits[5,6], sensor networks[7,8], and display backplanes[9]. The rapid expansion of flexible electronics has accordingly imposed varieties of new demands and challenges on the performance of TFTs, such as real-time interactivity, high-strain stability, and integrable multifunctionality, but nevertheless, simultaneously achieving high electrical performance and mechanical performance remains a giant obstacle for flexible TFTs in general. Although it is possible to mitigate the flexibility issue at the circuit level by engineering the interconnects with sophisticated shapes, this type of design nevertheless trades off a significant portion of the circuit area to accommodate the large interconnects, thereby limiting the integration density of circuits[10]. Therefore, it is highly desirable to have TFTs that are intrinsically flexible to constitute the circuits.

To this end, carbon nanotube (CNT) based TFTs have recently stood out for the intrinsic superior flexibility of CNTs[11,12], and particularly, not only the TFT channels but also the source, drain, and gate electrodes as well as the interconnects can be made of CNTs. This type of TFTs is also known as all-CNT (ACNT) TFTs. Owing to a fairly high carrier mobility together with superior mechanical flexibility and solution processability, ACNT TFTs have shown great promise for applications in flexible electronics[13,14]. Therefore, the flexible circuits built on ACNT TFTs can possibly enable many emerging applications in the 'smart' electronics and technologies. However, CNT TFTs commonly have an Achilles' heel at the gate dielectric, because the majority devices used brittle high-κ oxides (e.g., Al_2O_3 and HfO_2) as the gate dielectric and the oxides would break upon bending, resulting in current leakage[13,15–19]. Organic polymer dielectrics have been attempted as a replacement[20], but the device performance is fairly limited owing to a low κ value of the polymers and a thick layer required to ensure the insulating property[21]. Mixed composite dielectric of high-κ oxide and organic polymer could be made by solution process to balance the dielectric property and flexibility[22–24], but owing to the strong propensity of phase segregation at nanoscale, complete coating of a uniform thin dielectric layer on CNTs at a large scale was found to be extremely challenging if not impossible, which therefore seriously limits the use of the solution methods for circuit fabrication. On the other hand, a vapor-phase technique of initiated chemical vapor deposition (iCVD) was shown to grow polymer and composite dielectrics for TFTs[25–27], but the large-scale uniformity remains a serious concern for CVD in general.

To tackle the Achilles' heel issue of the gate dielectric, we herein propose a hybrid dielectric material of polyimide and Al_2O_3, which can be made by a scalable vapor deposition technique consisting of molecular layer deposition (MLD) and atomic layer deposition (ALD), namely MLD/ALD. In this approach, MLD and ALD were alternatively executed to grow the polyimide and Al_2O_3 layers, respectively, with subnanometer thickness, and thus a uniform mixing of the polymer and oxide could be achieved at a nanometer level. Such a level of mixing could endow the merits of both constitutes to the afforded hybrid dielectric, and indeed the afforded hybrid polyimide-Al_2O_3 dielectric was found to be of flexibility and high-κ dielectric property. With this hybrid dielectric, high-performance ACNT TFTs with truly intrinsic flexibility were realized, and these TFTs were further integrated to the basic circuit modules of inverters, ring oscillators,

[1]School of Electronic and Computer Engineering, Shenzhen Graduate School, Peking University, Shenzhen 518055, China. [2]School of Advanced Materials, Shenzhen Graduate School, Peking University, Shenzhen 518055, China. [3]These authors contributed equally: Qiuyue Huang, Jialiang Wang. ✉email: zhangm@ece.pku.edu.cn; wangxw@pkusz.edu.cn

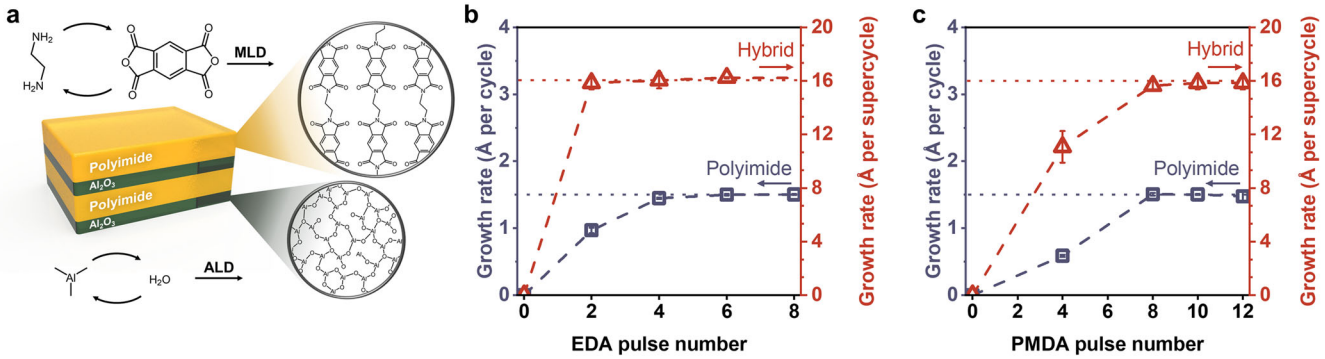

Fig. 1 Deposition scheme of the hybrid dielectrics. a Schematic illustration of the hybrid MLD/ALD process to deposit hybrid polyimide-Al_2O_3 films. Growth rates of the polyimide and hybrid films with respect to the pulse numbers of **b** EDA and **c** PMDA in each MLD cycle or MLD/ALD supercycle.

and logic gates to demonstrate the enormous possibilities of the intrinsically flexible TFTs for integrated circuits.

RESULTS

Deposition and characterization of hybrid dielectric

Hybrid polyimide-Al_2O_3 dielectric films were prepared by a hybrid MLD/ALD approach at 165 °C (Fig. 1a), where nanoscale sublayers of polyimide and Al_2O_3 were alternately deposited by MLD and ALD, respectively. While ALD of Al_2O_3 was well documented[28], the MLD of polyimide herein employed 1,2-ethylenediamine (EDA) and pyromellitic dianhydride (PMDA) as precursors and utilized the self-limiting imidization reaction between their anhydride and amine groups to achieve the layer-by-layer growth of the EDA-PMDA polyimide (Supplementary Fig. 1)[29,30]. Notably, while other types of polyimides could also be deposited by MLD[29], we chose EDA because it has a fairly high volatility and the afforded polyimide is transparent in the visible light range. The self-limiting behavior of the MLD growth of EDA-PMDA polyimide was first verified, by separately varying the pulse numbers of EDA and PMDA vapors in each MLD cycle[31], as shown in Fig. 1b, c. A saturated growth rate of 1.5 Å per cycle was observed as the pulse numbers of EDA and PMDA exceeded 4 and 8, respectively. The hybrid MLD/ALD process for the hybrid polyimide-Al_2O_3 films was conducted in a 'supercycle' fashion, where each supercycle consisted of 3 subcycles of MLD polyimide and 3 subcycles of ALD Al_2O_3. The hybrid process well retained the self-limiting nature of MLD and ALD. As also shown in Fig. 1b, c, a saturated growth rate of 16.0 Å per supercycle was observed as the pulse numbers of EDA and PMDA exceeded 2 and 8, respectively. Linear growth was also verified by varying the total supercycle number (Supplementary Fig. 2)[32].

The afforded hybrid polyimide-Al_2O_3 films were then characterized for material properties and compared with the pure polyimide films deposited by MLD. Figure 2a compares the typical X-ray photoelectron spectroscopy (XPS) survey spectra for a MLD polyimide film and a hybrid film. The spectrum of the MLD polyimide film exhibits prominent peaks of C, N, and O, and its atomic ratio, as extracted from the areal intensities, was found to be C:N:O = 12.3:2.1:4.0, which was fairly close to the ideal stoichiometry of the EDA-PMDA polyimide, that is, $[C_{12}N_2O_4H_6]_n$. High-resolution XPS spectra are provided in Supplementary Fig. 3, where a tiny Al *2p* peak was also observed. This Al peak was from the underneath Al_2O_3 buffer layer[33], which implies that the MLD polyimide film contained pinholes. As for the hybrid films, aside from similar C, N, and O peak features, pronounced Al peaks were observed in the XPS survey spectrum, which confirms the presence of Al_2O_3 in the hybrid film. The composition of the hybrid films was further analyzed by Rutherford back scattering (RBS)[34]. Figure 2b displays experimental and simulated RBS spectra for a hybrid film grown on a flat glassy carbon substrate, and the atomic ratio of the hybrid film was quantified to be N:O:Al = 2.0:6.1:1.4 (Supplementary Fig. 4). This ratio is well consistent with the addition of the stoichiometric ratios of N:O = 2:4 for the polyimide and O:Al = 3:2 for Al_2O_3. Note that RBS was not capable of directly detecting hydrogen, nor accurately quantifying carbon owing to the overwhelming carbon signal from the glassy carbon substrate. Nevertheless, we could assume the atomic ratio to be N:C:H = 2:12:6 as in the stoichiometric polyimide ($[C_{12}N_2O_4H_6]_n$) and calculate the density of the hybrid films to be 1.45 g cm^{-3}, which is comparable to that of the commercial ODA-PMDA polyimide (1.42 g cm^{-3}) (ODA = 4-4′-oxydianiline)[35]. Atomic force microscopy (AFM) was used to examine the surface morphology of the polyimide and hybrid films. As shown in Fig. 2c, d, the polyimide film was relatively rough (2.64 nm in rms roughness) and contained pinholes; whereas the hybrid film was much smoother with no observable pinholes, and its rms roughness was only 0.29 nm. A smooth film is a prerequisite for the gate dielectric applications.

Fourier transform infrared spectroscopy (FTIR) was further used to analyze the chemical bonding information of the polyimide and hybrid films. As shown in the upper panel of Fig. 2e, the FTIR spectrum of the polyimide film shows a pair of absorption peaks at 1778 and 1714 cm^{-1} and a separate peak at 1378 cm^{-1}, which correspond to the symmetric and asymmetric C=O stretching and the C−N−C stretching vibrations of the imide group, respectively[29,36,37]. Notably, no appreciable absorption was observed between 1700 and 1500 cm^{-1}, which is a characteristic absorption range for polyamic acid, a possible incompletely imidized product (typically at 1650 and 1680 cm^{-1} for amide and carboxylic C=O stretching, respectively, and at 1700–1500 cm^{-1} for carboxylate C=O stretching)[38,39]. The negligible intensity of the polyamic acid absorption suggests that the MLD polyimide had a fairly high degree of imidization[37,38]. The high degree of imidization is favored for dielectric applications, as it can promote the insulating properties and enhance the stability against degradation upon long-time air exposure[40]. To achieve a high degree of imidization, conventional solution processes usually require a thermal curing treatment typically at 350 °C[41]. In contrast, the MLD of the polyimide herein needed only a process temperature to be as low as 165 °C, which is well compatible with many plastic substrates, such as polyethylene terephthalate (PET) and polyethylene naphthalate (PEN), for flexible electronic applications. The lower panel of Fig. 2e shows the FTIR spectrum of the hybrid film. Compared to the pure polyimide, the spectrum of the hybrid film contains two additional broad strong bands at 1000–500 cm^{-1} and 1700–1500 cm^{-1}. The band at 1000–500 cm^{-1} corresponds to the vibrational absorption of Al_2O_3 clusters[42–44]; whereas the band at 1700–1500 cm^{-1} can be assigned to the multiple C=O

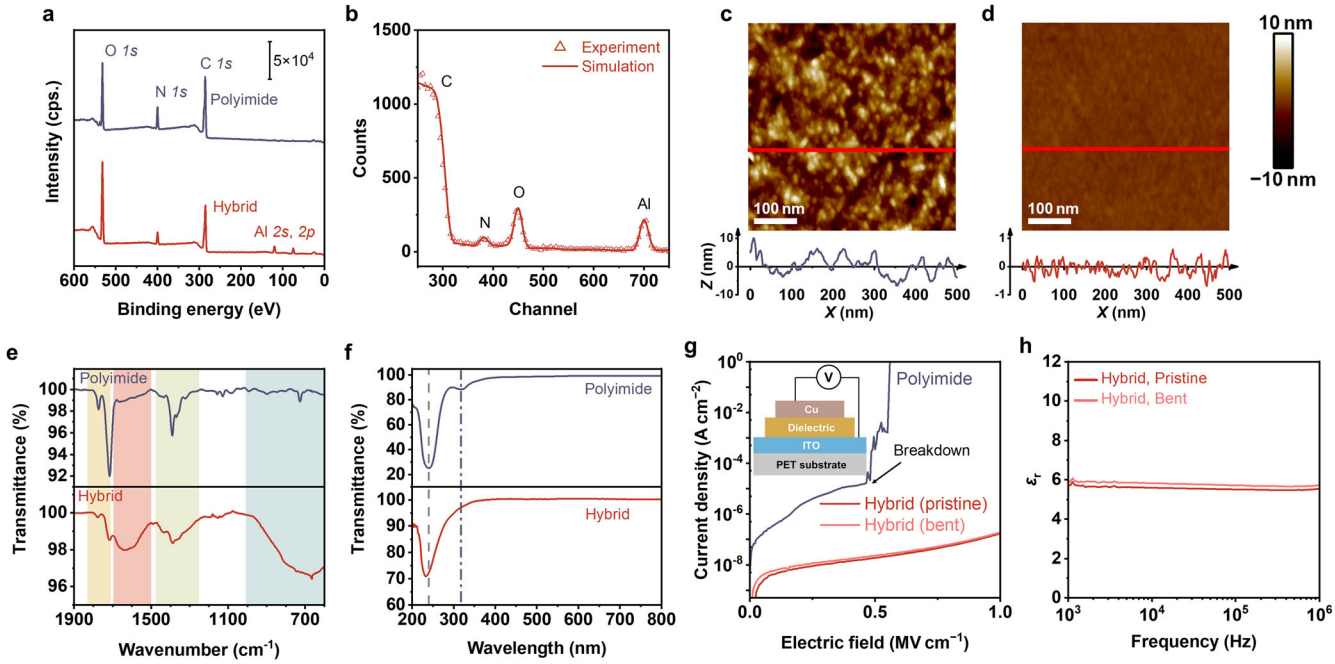

Fig. 2 Material characterization of the polyimide and the hybrid films. a XPS survey spectra of a polyimide film and a hybrid film. **b** RBS experimental and simulated spectra for a hybrid film grown on a flat glassy carbon substrate. AFM images of **c** a polyimide film and **d** a hybrid film grown on flat Si wafer substrates. Bottom profiles present the height traces of the line sections labeled in the above images. **c** FTIR spectra of a polyimide film and a hybrid film grown on KBr plates. **f** UV–vis spectra of a polyimide film and a hybrid film grown on glass substrates. **g** Leakage current of the MIM capacitors with the polyimide or hybrid dielectric (inset schematically illustrates an MIM capacitor structure). **h** ε_r of the hybrid dielectric as a function of frequency.

stretching modes of carboxylic and carboxylate groups[39,42,45]. The carboxylic and carboxylate groups are presumably the terminal groups of the polyimide chains, and they can coordinate to the surface Al atoms of Al_2O_3 clusters to various degrees. Consequently, the 1700–1500 cm^{-1} band became considerably broader than the absorption peaks of the well-defined imide group. Therefore, the FTIR results well captured the microstructural information of the hybrid polyimide-Al_2O_3 material.

UV-vis spectroscopy was further used to analyze the polyimide and hybrid films. As shown in Fig. 2f, both films were fairly transparent (transmittance > 98%) in the visible light range (400–800 nm), and the major absorption peaks were in the UV range at ca. 240 nm. The optical gaps of the polyimide and hybrid films were extracted from the absorption edges to be 4.52 and 4.27 eV (Supplementary Fig. 5), respectively, and these numbers are much larger than that of the commercial ODA-PMDA polyimide (ca. 2.6 eV) owing to the use of the non-aromatic diamine (EDA)[46,47]. Therefore, the synthesized polyimide and hybrid films are highly suited for transparent electronic applications. It is also worth noting that, in contrast to the spectrum of the hybrid film, the polyimide spectrum exhibits an additional adsorption shoulder at 320 nm. As discussed in the following, this shoulder peak is indicative of polymer aggregation, which can lead to the leakage of electric current through the dielectric film.

The film dielectric properties were evaluated via metal-insulator-metal (MIM) capacitors, which were fabricated on ITO-coated PET substrates using the polyimide or hybrid film as the dielectric. As shown in Fig. 2g, with the polyimide dielectric, the capacitor exhibited a relatively high leakage current of up to 1×10^{-5} A cm^{-2} at low field and broke down at approximately 0.5 MV cm^{-1}. In contrast, the capacitor with the hybrid dielectric showed a fairly good insulating property with a leakage current of only 1.1×10^{-7} A cm^{-2} at 1 MV cm^{-1}. Moreover, the hybrid dielectric could also withstand the bending to a small radius of 5 mm (Fig. 2g), as the capacitor after the bending showed only marginal increase in the leakage current. On the contrary, the Al_2O_3 dielectric failed upon bending, as the MIM capacitor made of the ALD Al_2O_3 dielectric was shorted after the above bending test (Supplementary Fig. 6). The relative dielectric constant (ε_r) of the hybrid film was obtained to be 5.8, from the capacitance-frequency response (Fig. 2h), and this number is higher than the value of commercial Kapton polyimide (3.9), owing to the incorporation of high-κ Al_2O_3[42].

DFT analysis

To further understand the electronic structures of the polyimide dielectric, we performed density-functional theory (DFT) calculation on a model molecule of *N*,*N*′-dimethyl pyromellitic diimide to analogize the conjugated unit of the EDA-PMDA polyimide (Fig. 3a inset)[47]. The dimer of this model molecule was also calculated to investigate the intermolecular interaction and packing effect. Figure 3a shows the energy levels of the monomer and dimer with optimized geometries (Supplementary Fig. 7), and detailed spatial distributions of HOMOs and LUMOs are depicted in Supplementary Fig. 8. Notably, in the dimer the two molecules are parallel packed with considerable shift perpendicular to the molecule chain; therefore, the intermolecular interaction is weak, and the LUMO (HOMO−1) and LUMO+1 (HOMO) of the dimer can be roughly viewed as the in-phase and out-of-phase combinations of the monomer LUMOs (HOMOs), respectively. Indeed, the energy splits, which reflect the strength of the intermolecular interaction, were calculated to be fairly small as 0.19 and 0.03 eV for the pairs of LUMO/LUMO+1 and HOMO/HOMO−1, respectively. Comparatively, the former value is greater than the latter, which suggests that LUMO is more susceptible to the molecular packing. Indeed, the spatial distribution of the monomer LUMO is more extended than HOMO (Supplementary Fig. 8), and therefore the overlap of the monomer LUMOs in an aggregate can be critically related to the leakage current property of the polyimide film, as it can provide an electron hopping path among the monomers in the film.

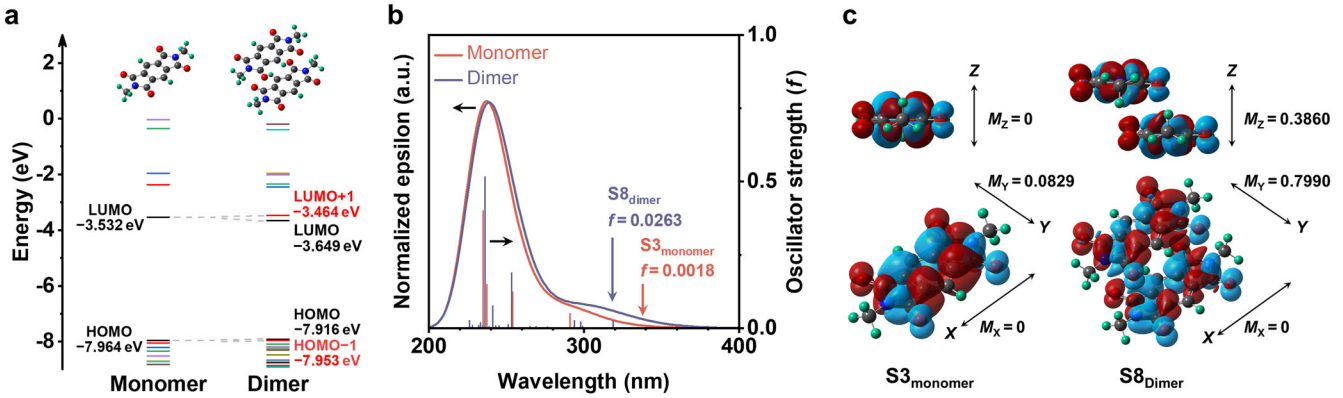

Fig. 3 DFT calculation of *N,N′*-dimethyl pyromellitic diimide as a model molecule for the polyimide. a Energy levels of the monomer and dimer. **b** UV–vis spectra calculated based on TD-DFT formalism. **c** Spatial distributions of the monomer ($S3_{monomer}$) and dimer ($S8_{dimer}$) transition densities. M_X, M_y, and M_z represent the cartesian components of the transition dipole moments.

Time-dependent DFT (TD-DFT) formalism was further employed to calculate the vertical transitions and UV–vis spectra of the monomer and dimer. Figure 3b shows the calculated UV–vis spectra, and the spatial distributions of the hole and electron orbitals associated with the transitions are provided in Supplementary Figs. 9 and 10. Both the monomer and dimer UV–vis spectra exhibit a major absorption at 239 nm, which is consistent with the experimental spectra shown in Fig. 2f. In addition, the calculated dimer spectrum also displays an extra prominent shoulder at the high wavelength side, which resembles the feature observed in the experimental polyimide spectrum (Fig. 2f). From TD-DFT calculation, this shoulder peak originates from the transition of the ground state to the $S8_{dimer}$ state (319 nm, $f = 0.0263$), and the analysis of the hole and electron orbitals of this transition reveals that this transition is essentially from HOMO/HOMO−1 to LUMO/LUMO+1. In fact, the HOMO-to-LUMO transition also exists in the calculated monomer spectrum ($S3_{monomer}$, 338 nm, $f = 0.0018$), but its oscillator strength is too weak to be visible in Fig. 3b. Apparently, the HOMO-to-LUMO transition is considerably enhanced by the dimer stacking. We further calculated the transition densities to the $S3_{monomer}$ and $S8_{dimer}$ states by Multiwfn[48,49]. As shown in Fig. 3c, the distribution of the transition density to $S3_{monomer}$ is symmetric in both *X* and *Z* direction, leaving only a small non-zero transition dipole moment (*M*) in the *Y* direction[47]. On the other hand, owing to the intermolecular interaction, the distribution of the transition density to $S8_{dimer}$ is no longer symmetric in the *Z* direction and is also more extended over the two monomers in the *Y* direction. Therefore, the overall transition dipole moment is significantly enhanced by the dimer stacking.

On the basis of the DFT analysis, the shoulder peak at 320 nm in the UV-vis spectra is a good indicator of the π-π stacking of the conjugated units in the polyimide. As the π-π stacking can result in an unwanted path for electron hopping, the smaller the shoulder peak, the better the insulting property should be for the dielectric film. Indeed, the hybrid film with no observable shoulder peak displayed a much smaller leakage current than the pure polyimide film (Fig. 2g). Therefore, the incorporation of the inorganic Al_2O_3 in the hybrid material is of critical importance to suppress the propensity of the π-π stacking and thereby enhance the film insulting property.

Intrinsically flexible, hybrid-dielectric ACNT TFTs

Using the above hybrid dielectric as the gate dielectric, we prepared all-CNT (ACNT) TFTs, which are intrinsically flexible. The source, drain, and gate electrodes of TFTs were made of metallic CNTs (MCNTs), and the channels were made of semiconducting CNTs (SCNTs) with 99.9% purity as purchased. Compared with the conventional metal electrodes, the MCNT electrodes can withstand a much larger bending strain and therefore are better suited for the flexible devices. All the CNT layers were prepared by spin coating, which was carefully developed to achieve high uniformity of the density, thickness, and connectivity of SCNTs in the channels and good metal-semiconductor contact at the source and drain electrodes. Details of the device fabrication are described in Methods. Figure 4a schematically illustrates the structure of TFT, and Fig. 4b shows a top-view scanning electron microscopy (SEM) image of TFT. Figure 4c shows a schematic illustration of the channel CNTs being conformally coated by the hybrid dielectric via the above hybrid MLD/ALD process[50,51], and the complete coating was well observed by cross-sectional SEM, as shown in Fig. 4d. Notably, because all the device components were made of flexible materials, and the fabricated devices and circuit arrays are therefore intrinsically flexible. Therefore, they could be conformally attached on a human wrist, rolled on a finger, or twisted to a large degree, as shown in Fig. 4e.

Electrical properties of the afforded TFTs are characterized in the following. Figure 4f, g shows the transfer and output characteristics of a representative TFT. As the gate voltage (V_g) varied from −5 to 3 V, the gate leakage current ($|I_g|$) remained below 10 pA, which indicates a good insulation property of the thin hybrid dielectric. The on-off current ratio (I_{on}/I_{off}) of the device was able to reach a high level of 3.62×10^4 ($I_{on} = 81.3$ nA, $I_{off} = 2.24$ pA), and both the threshold voltage (V_{th}) and subthreshold swing (*SS*) were found to be fairly low as −0.6 V and 0.17 V dec^{-1}, respectively, thanks to the employment of the thin high-*κ* gate dielectric. Low V_{th} and *SS* are of vital importance to achieve the switching function at low operating voltage. In addition, the maximum transconductance density (g_m/W) in the linear region ($V_d = -0.1$ V) was able to reach a high value of 2 nS μm^{-1}, which suggests that a high driving capability can be simultaneously achieved with high-speed switching function. In the associated output characteristics (Fig. 4g), we observed an ideal linear and saturation behavior of the current, which suggests a good metal-semiconductor contact at the source and drain electrodes. We also evaluated the bias and thermal stability of TFTs. As shown in Supplementary Fig. 11, both I_{on} and I_{off} remained almost constant under biased V_g for 1000 s, which reflects a good bias stability of TFTs. As the temperature was elevated from room temperature (20 °C) to 180 °C, the I_{on}/I_{off} ratio remained above 10^3, and the leakage current was below 35.4 fA μm^{-2}, which indicates that the devices were of a fairly good thermal stability. The good electrical bias stability and thermal stability are highly desirable for broad applications of TFTs.

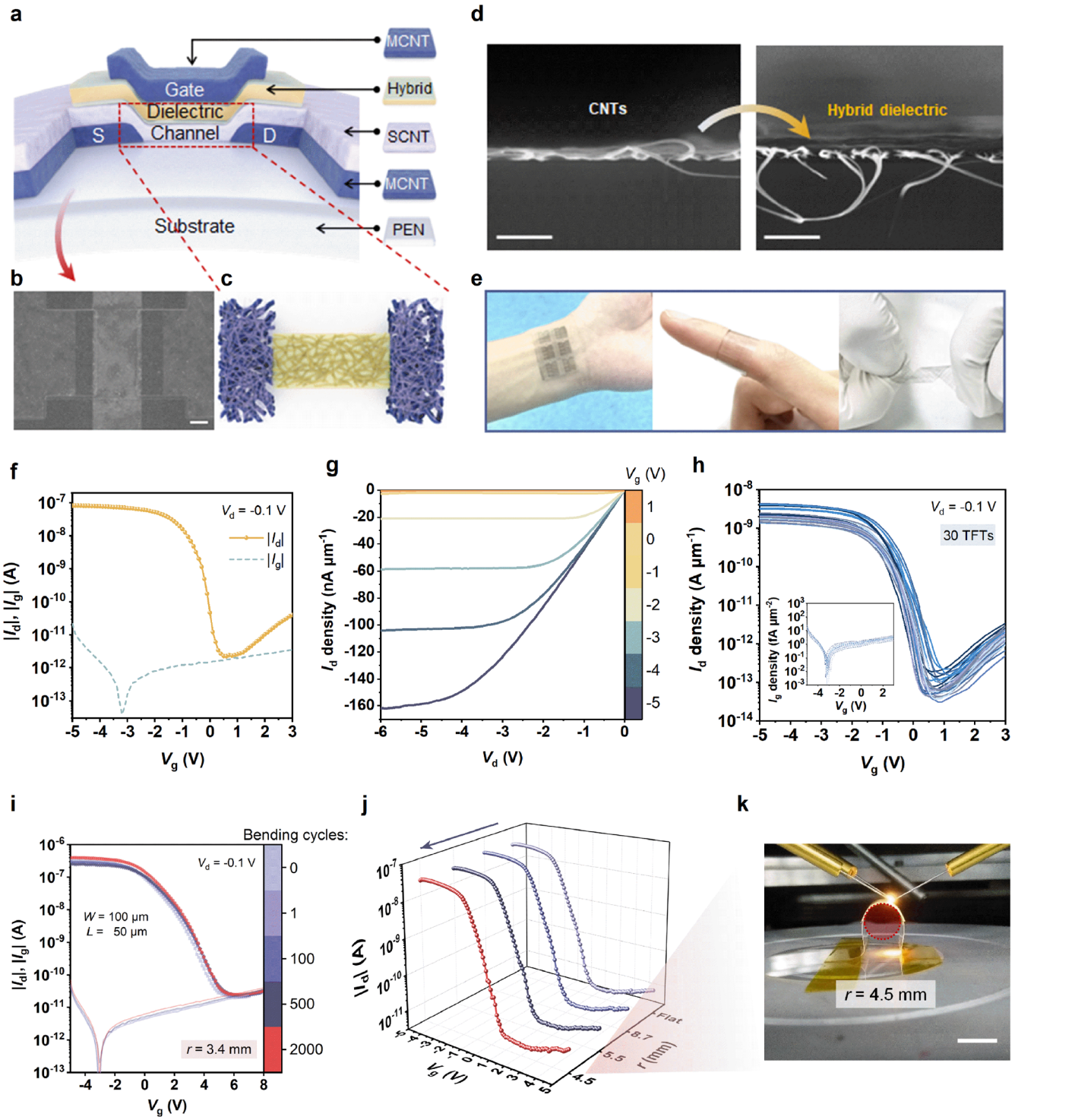

Fig. 4 Device performance of ACNT TFTs with the hybrid dielectric. a Schematic illustration and **b** top-view SEM image of TFT (scale bar 20 μm). **c** Schematic illustration and **d** SEM images showing the channel CNTs being conformally coated by the hybrid dielectric (scale bar 400 nm). **e** Photographs showing that the TFT circuits can be attached on a human wrist, rolled on a finger, or twisted to a large degree. **f** Transfer and **g** output characteristics of a representative TFT ($W = 20$ μm, $L = 50$ μm). **h** Transfer characteristics of 30 TFTs ($L = 50$ μm, $V_d = -0.1$ V). Inset shows the associated gate leakage current density. **i** Evolution of transfer characteristics for a TFT over 2000-cycle bending test ($r = 3.4$ mm). **j** Transfer characteristics measured during the in-situ bending test. **k** Photograph showing the in-situ bending test with a curvature radius of 4.5 mm (scale bar 1 cm).

We further analyzed the device-to-device variation, as a uniform device performance is essential for circuit integration. Figure 4h plots the transfer characteristics of 30 TFT devices fabricated as a matrix. All the transfer curves overlapped quite well, which indicates a fairly good uniformity of the device performance. Statistical analysis gave out a fairly small V_{th} of -0.67 ± 0.14 V, a high I_{on}/I_{off} of $10^{4.54\pm0.26}$, and a fairly low SS of 0.26 ± 0.05 V dec^{-1}, together with fairly low gate leakage current density ($|I_g|/WL$) uniformly below

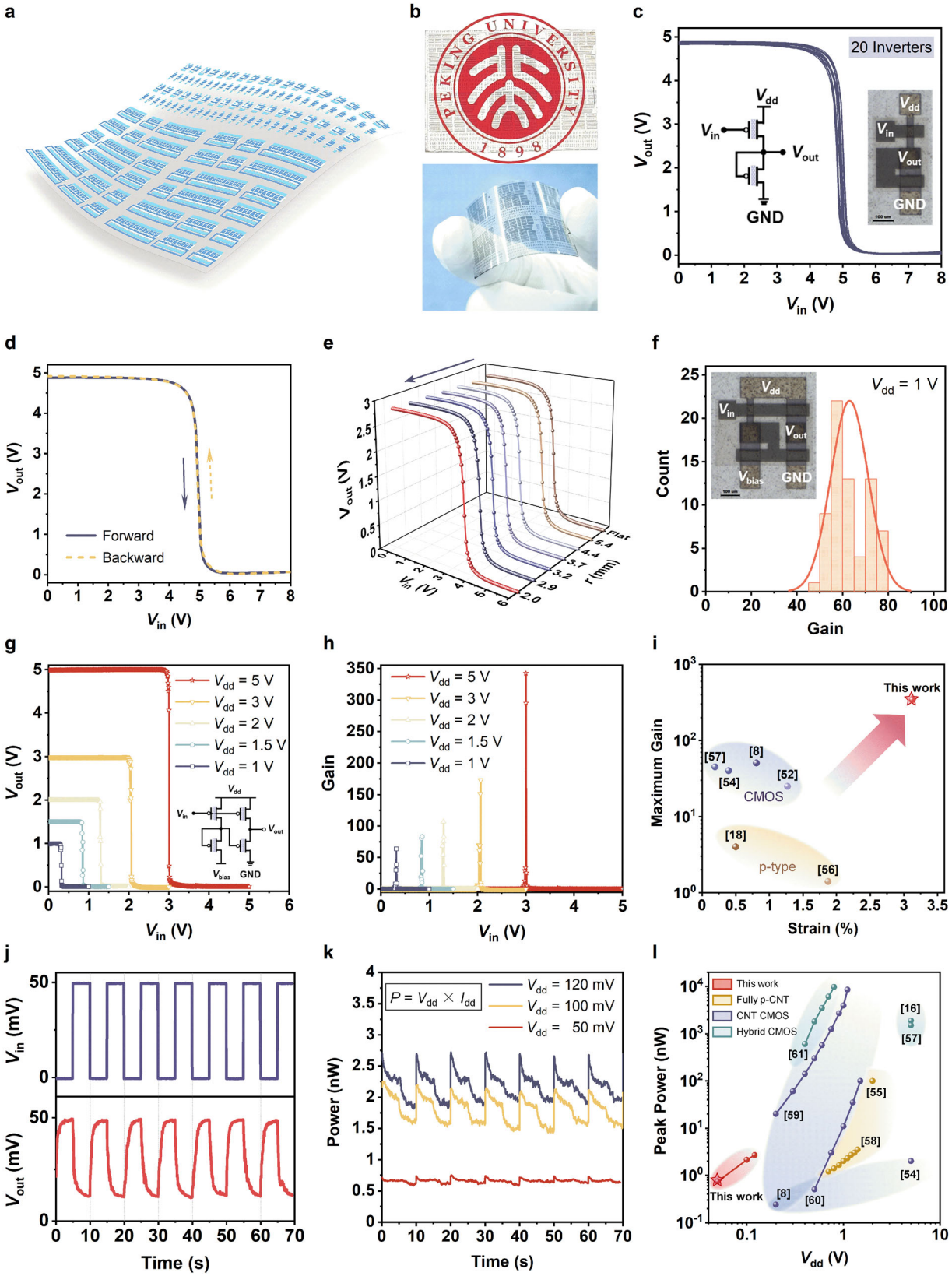

20 fA μm^{-2}. Standard deviations of these parameters were all within 20%, which is also small for ACNT TFTs[14,15,52,53].

To further evaluate the device flexibility, we carried out a bending test by bending the TFT devices to a curvature radius (r) of 3.4 mm for up to 2000 cycles. As shown in Fig. 4i, the good transfer characteristics were well maintained over the entire bending test, as the changes of SS, I_{on}/I_{off}, and V_{th} were all fairly small as 10.9, 7.2, and 7.8%, respectively. More importantly, we

Fig. 5 Integrated circuits based on intrinsically flexible TFTs. a Schematic illustration and **b** photographs of the integrated circuit arrays of inverters, ring oscillators, and logic gates. **c** Voltage transfer characteristics of 20 inverters ($V_{dd} = 5$ V). Inset shows an optical image and the circuit diagram of the inverter (scale bar 100 μm). **d** Forward and backward sweeps of voltage transfer characteristics. **e** Evolution of voltage transfer characteristics over sequential bending test to a curvature radius of 2 mm. **f** Histogram of gain over 70 pseudo-CMOS inverters ($V_{dd} = 1$ V). Inset shows an optical image of the pseudo-CMOS inverter. **g** Voltage transfer characteristics and **h** gain of a pseudo-CMOS inverter at various V_{dd} from 5 to 1 V. Inset shows the circuit diagram of the pseudo-CMOS inverter. **i** Benchmarking of the gain and bending strain with the state-of-the-art CNT-based flexible inverters. **j** Input and output waveforms of a pseudo-CMOS inverter operated at 50 mV. **k** Power consumption of the pseudo-CMOS inverter at various low V_{dd} from 120 to 50 mV. **l** Benchmarking of the peak power consumption and operation voltage with the state-of-the-art CNT-based inverters.

observed no appreciable increase in the leakage current, which indicates that the hybrid dielectric layer could indeed withstand the bending test. In situ bending test was further carried out. As shown in Fig. 4j, k, the device electrical properties were characterized when the devices were bent to the curvature radii of 8.7, 5.5, and 4.5 mm. All the acquired transfer curves were roughly the same, and in particular, the changes of *SS*, I_{on}/I_{off}, and V_{th} were only as small as 4.9, 12.0, and 8.6%, respectively, as the devices were bent to the smallest curvature radius of 4.5 mm. These results indicate that the electrical performance of TFTs was stable even at a largely bent state. Therefore, we have so far demonstrated that, with the employment of a thin intrinsically flexible hybrid dielectric, which could be conformally coated on the CNT channel by MLD/ALD, highly flexible TFTs with superior electrical performance and bending tolerance can be well realized.

Inverters, ring oscillators, logic gates, and amplifiers

Based on the above intrinsically flexible TFTs, we further explored their applications in flexible integrated circuits. As illustrated Fig. 5a, we demonstrated three types of basic digital integrated circuit modules of inverters, ring oscillators, and logic gates, as follows. As the photographs shown in Fig. 5b, the fabricated circuits were transparent and flexible. Detailed fabrication steps are described in Methods.

We first employed the TFTs to build inverters, which are the foundation unit of digital circuits. We assessed two types of the configurations for the inverters, which were the zero-V_{gs} and pseudo-CMOS configurations. The zero-V_{gs} configuration has a simpler structure and therefore is desirable for high integration density; whereas the pseudo-CMOS configuration can generally deliver better inverter characteristics, such as higher gain, lower power consumption, and larger noise margin. An inverter with zero-V_{gs} configuration is shown in Fig. 5c inset, and Fig. 5c compares the voltage transfer characteristics (VTC) over 20 inverters. The output swing and gain were found to be fairly uniform, particularly the deviation of switching voltage was only 1.7%, and also no hysteresis was observed during the forward and backward V_{in} sweeps (Fig. 5d). All these merits are of high importance for circuit integration. The flexibility of the inverter was further assessed by bending the inverter to a curvature radius of down to 2 mm. As shown in Fig. 5e, the VTC of the inverter exhibited no appreciable change upon the bending, which highlights the flexibility of the afforded inverters. Notably, in prior studies of CNT-based inverters, good flexibility has rarely been demonstrated at the circuit level, possibly owing to the use of inherently brittle oxide dielectrics (Table S1). Moreover, the herein shown small bending radius of 2 mm is satisfactory to most demands in contemporary application scenarios, such as rollable displays, wearable electronics, and electronic skin applications[54]. In addition, given the herein used PEN substrate thickness of 125 μm, the bending radius of 2 mm corresponded to 3.1% of tensile strain imposed on the inverter, and the tolerance to such level of strain was quite good at the circuit level.

As for the pseudo-CMOS configuration, Fig. 5f shows the distribution of the gain over 70 pseudo-CMOS inverters operated at $V_{dd} = 1$ V, and a fairly high level of gain of 63.0 on average and 77.8 for the champion was obtained. Also, a large noise margin of up to 88.2% of $V_{dd}/2$ was achieved under the condition of $V_{dd} = 1$ V (Supplementary Fig. 12). The inverters were also able to be well operated over a wide range of V_{dd} from 50 mV to 5 V. As shown in Fig. 5g, h, when a high V_{dd} of 5 V was applied, the inverter gain was able to reach 342.5, which is a record high number among the reported CNT-based flexible inverters (Table S1)[8,13,15–18,52,54–57]. As compared in Fig. 5i, the maximum gain and bending strain achieved in this work greatly outperformed the numbers of the state-of-the-art CNT-based flexible inverters. As a large gain is essential for signal regeneration and amplification, the intrinsically flexible pseudo-CMOS inverters will have great applications in fast switching circuits, logic processing units, and output buffer elements. Moreover, merited from the low threshold and superior gate controllability of the constituted TFTs, the inverters were also able to operate under a very low voltage of 50 mV with peak and dynamic powers of only 0.74 and 0.66 nW, respectively (Fig. 5j, k). This operation voltage is by far the lowest for CNT-based inverters, as compared in Fig. 5l with fully p-type CNT inverters[55,58], CNT CMOS inverters[8,54,59,60], and hybrid CMOS inverters using p-type CNT TFT and other n-type TFT[16,57,61]. Therefore, the devices by our approach are also highly promising for ultralow power applications, such as wearable electronics with low-voltage power supply from ambient energy harvesters (usually <1 V)[62].

Further, we fabricated ring oscillators and logic gates based on the intrinsically flexible ACNT TFTs. Figure 6a illustrates the layouts of a 3-stage and a 7-stage ring oscillators, and the output waveforms are shown in Fig. 6b, c. The 7-stage ring oscillator was assessed with a range of working voltage (i.e., V_{dd}) from 1.3 to 5 V, and stable oscillation output was obtained for all the assessed voltages (Fig. 6b). Figure 6c shows the output waveform of the 3-stage ring oscillator under $V_{dd} = 3$ V, and the oscillation was also stable with a high frequency of 1.75 kHz. The kHz-level frequency of oscillation is satisfactory for use in display applications and electrical signal sensing, such as heart rate monitoring and body movement detection. The successful realization of the multi-stage ring oscillators is particularly important, as it clearly indicates a high yield and circuit-level uniformity of the constituted ACNT TFTs fabricated by our approach. Moreover, a full set of logic gates, including NAND, NOR, XOR, and AND, were fabricated based on the above ACNT TFTs. As shown in Fig. 6d–h, all these logic gates showed correct logic functions, which can be further applied for complex logic control and process circuits. In addition, it is worth noting that the herein NAND and NOR gates adopted a pseudo-CMOS configuration with bias, and therefore an ideal full-swing output was achieved; on the other hand, the XOR and AND gates used a transmission gate configuration, which could substantially reduce the required number of TFTs and therefore is desirable for high integration density. The successful realization of both configurations suggests a broad applicability of our approach, as it can allow for a greater freedom in circuit design to utilize their individual advantages.

Aside from being the foundation units of digital circuits, the intrinsically flexible high-gain low-voltage inverters are also of great potentials in analog circuits. For instance, there are many physiological signals in human body, which carry important information about health conditions, but the amplitude of these

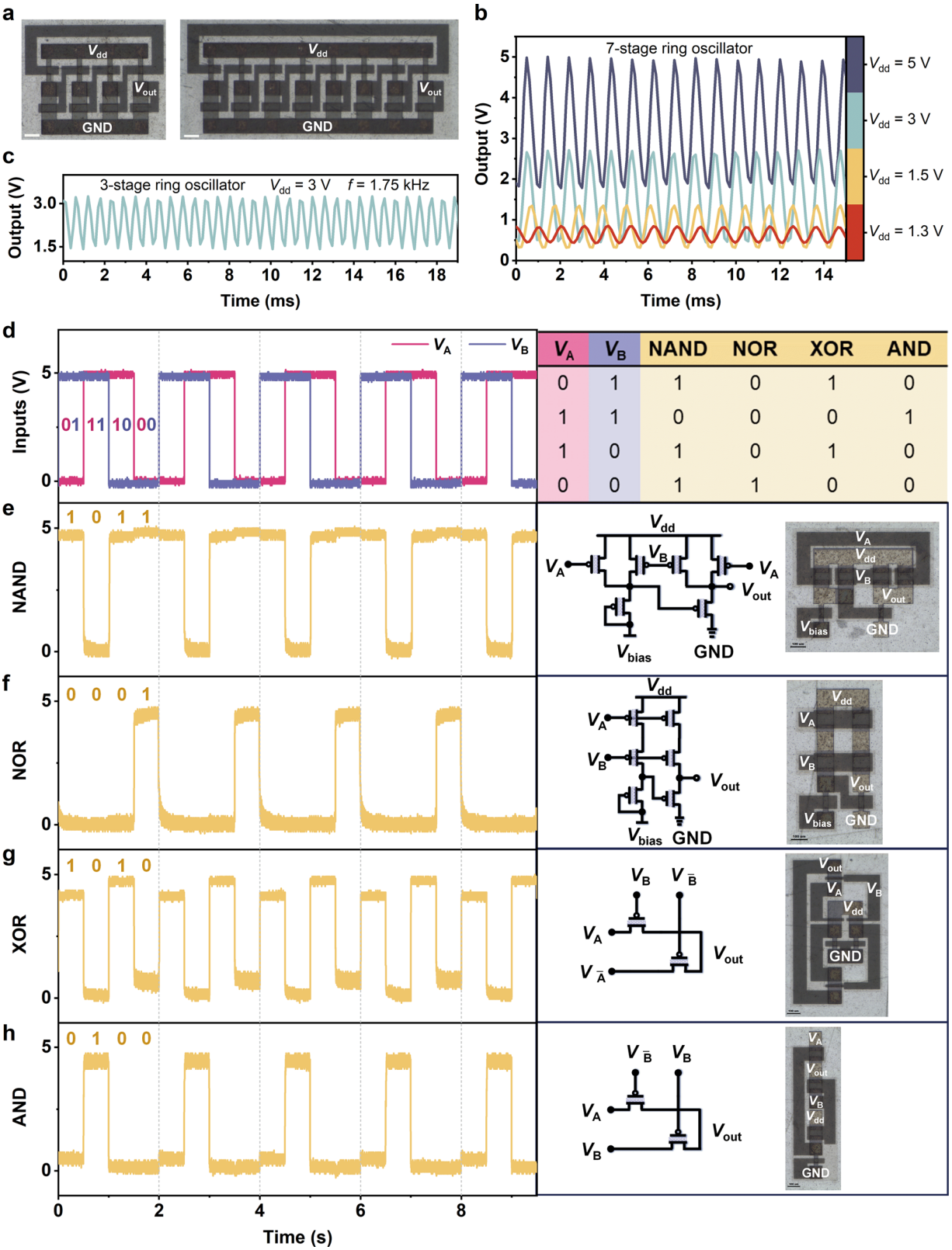

V_A	V_B	NAND	NOR	XOR	AND
0	1	1	0	1	0
1	1	0	0	0	1
1	0	1	0	1	0
0	0	1	1	0	0

Fig. 6 Ring oscillators and logic circuits. a Optical images of the 3-stage and 7-stage ring oscillators (scale bar 100 μm). **b** Output waveform of the 7-stage ring oscillator with various V_{dd} from 5 to 1.3 V. **c** Output waveform of the 3-stage ring oscillator with an oscillation frequency of 1.75 kHz. **d** Input, truth table, and output waveforms of the **e** NAND, **f** NOR, **g** XOR, and **h** AND gates. The corresponding optical images and circuit diagrams are shown on the right (scale bar 100 μm).

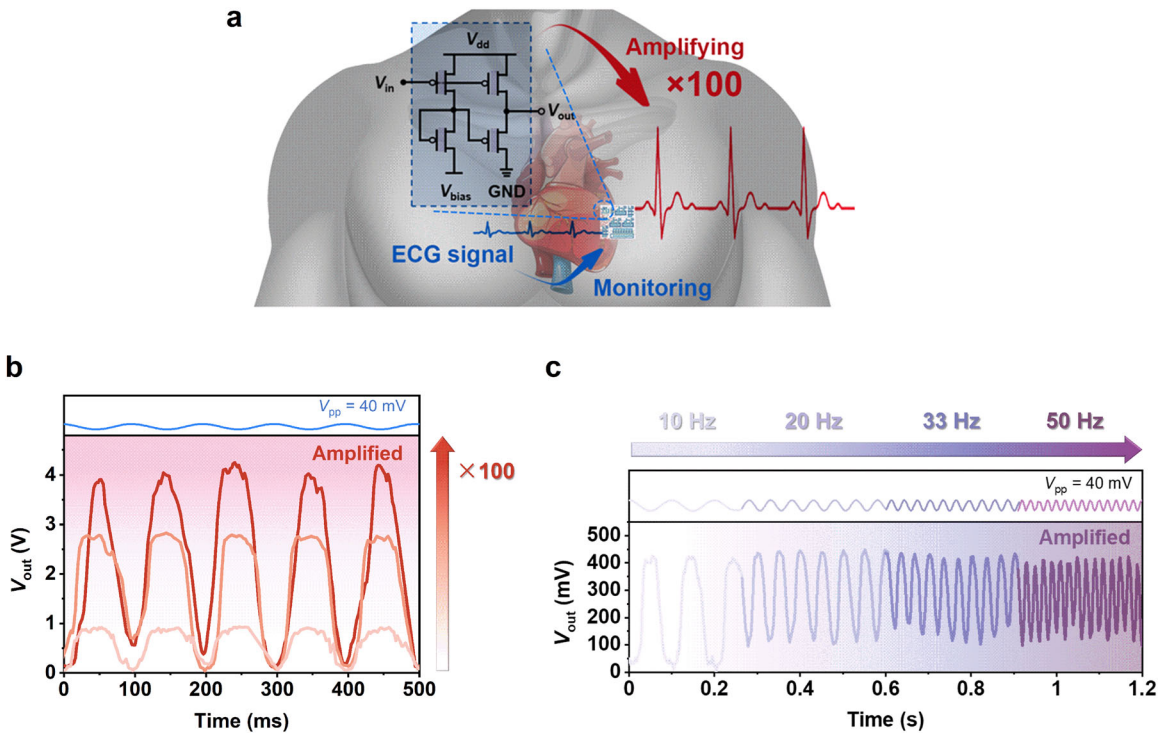

Fig. 7 Amplifier for ECG monitoring. a Illustration of the ECG monitoring using an analog amplifier made of the intrinsically flexible ACNT circuits. **b** Output signals of the amplifier showing as many as 100 times of signal amplification ($V_{pp} = 40$ mV, $V_{dd} = 1$, 3, and 5 V). **c** Amplifier output with various input signal frequencies of 10–50 Hz ($V_{dd} = 0.5$ V).

signals is usually rather weak (millivolt range), and therefore signal amplification is crucial for effectively signal post-processing and diagnosis[63]. Electrocardiographic (ECG) signal is one of these signals; it is generated by cardiac motion and usually on the order of millivolt in amplitude. As a demonstration, we applied our devices to work as a small-signal amplifier for the ECG monitoring. We fabricated the amplifier based on the ACNT inverter (Fig. 7a), and, as shown in Fig. 7b, the amplifier showed its amplification capabilities for small analog signals (40 mV). The gain of signal was achieved as high as 100, and the waveform was also well retained. As shown in Fig. 7c, the amplification behavior was also stable against the variation of the input signal frequency from 10 to 50 Hz. By integrating the analog and digital circuits for signal processing, controlling, and driving, wearable ECG monitoring system can be made in full of the intrinsically flexible ACNT circuits. Therefore, these ACNT circuits are of particular promise for the IoT era applications of wearable electronics, where small signal processing is paramount, such as real-time health monitoring and wearable motion sensing.

DISCUSSION

In this work, we proposed and demonstrated that a hybrid dielectric material, consisting of the polyimide and Al_2O_3, could well serve as the gate dielectric for intrinsically flexible integrated circuits. The constituent organic polyimide provided superior flexibility while the inorganic Al_2O_3 enhanced the dielectric constant and insulating property, and thus the afforded organic-inorganic hybrid dielectric was of intrinsic flexibility. The polyimide-Al_2O_3 dielectric was synthesized by a hybrid MLD/ALD approach, which is scalable and compatible with standard integrated circuits processing. In this synthesis approach, MLD and ALD were alternatively executed to deposit the polyimide and Al_2O_3 layers, respectively, with subnanometer thickness, which enabled a fairly uniform mixing of the polymer and oxide. Thorough material characterizations of the afforded polyimide-Al_2O_3 dielectric were carried out together with detailed DFT analysis to understand the interplay of molecular stacking, oxide incorporation, and dielectric properties.

The hybrid dielectric was further employed to fabricate intrinsically flexible ACNT TFTs and integrated circuits. Owing to the good gate dielectric property along with well-developed device structure and fabrication process, the afforded TFTs showed a small V_{th} of -0.67 ± 0.14 V, a high I_{on}/I_{off} of $10^{4.54\pm0.26}$, a low SS of 0.26 ± 0.05 V dec^{-1}, a low gate leakage current density uniformly below 20 fA μm^{-2}, and circuit-level uniformity. Besides, the TFTs were able to withstand 2000 cycles of bending to a small curvature radius of 3.4 mm, which clearly indicated their bending tolerance. Based on these high-performance TFTs, intrinsically flexible ACNT integrated circuits could be constructed. We demonstrated that well-behaved inverters, ring oscillators, and logic gates, including NAND, NOR, XOR, and AND, could be made of these intrinsically flexible TFTs. In particular, the afforded inverters could withstand a fairly high tensile strain of 3.1 % and exhibit a remarkably high gain of 342.5. The realization of such a high gain is an indicator of high-level performance uniformity over the TFTs, and it is also merited from the design of the zero-V_{gs} and pseudo-CMOS configurations (Supplementary Fig. 13). Ultralow voltage (50 mV) operation was also feasible, which is of great promise for low-power applications. The device-to-device variation was small, which have enabled the successful realization of the multi-stage ring oscillators. Aside from the digital circuits, an analog small-signal amplifier could also be built from the high-gain low-voltage ACNT inverter. With this amplifier, small millivolt signals could be amplified by 100 times. Therefore, the intrinsically flexible ACNT circuits are of particular promise for the IoT era applications that rely heavily on small signal processing, such as real-time health monitoring and wearable motion sensing.

METHODS

Preparation and characterization of the polyimide and hybrid dielectric films

Both the polyimide and hybrid films were deposited in a home-built tubular ALD/MLD reactor[64,65]. The polyimide films were deposited by MLD from 1,2-ethylenediamine (EDA) and pyromellitic dianhydride (PMDA) as the precursors, and the hybrid films were deposited by alternately MLD of the polyimide and ALD of Al_2O_3 from trimethylaluminum (TMA) and water vapor (i.e., hybrid MLD/ALD approach). During deposition, EDA, TMA, and water were kept at room temperature (25 °C), while PMDA was heated to 163 °C. Purified N_2 gas was used as the carrier gas to assist the precursor delivery, and it was also used as the purge gas. The chamber pressure during purging was approximately 1 Torr. The deposition temperature was at 165 °C, which was higher than the PMDA vaporization temperature to avoid its condensation. The MLD of the polyimide was conducted in close-valve mode. Unless otherwise specified, 2 pulses of EDA vapor and 10 pulses of PMDA vapor were dosed in each MLD cycle, which corresponded to the exposures of 0.033 and 0.063 Torr s for EDA and PMDA, respectively. Long purge time of 100 s was employed to ensure complete removal of the byproduct and excess precursors. The ALD of Al_2O_3 was processed in flow-through mode, where the exposures of TMA and water vapor in each ALD cycle were 0.014 and 0.064 Torr s, respectively. The hybrid MLD/ALD process was performed in a supercycle approach, where each supercycle consisted of 3 MLD cycles of the polyimide and 3 ALD cycles of Al_2O_3. To interrogate the film growth behavior and material properties, all the films were deposited on ALD Al_2O_3-coated substrates to ensure a same initial surface condition for film growth. These substrates were thermal oxide Si wafers (i.e., Si wafers with 300 nm thermally grown SiO_2), low-resistivity Si(100) wafers (p^{++}, 0.1–0.9 mΩ cm), glassy carbon plates, KBr plates, and glass substrates, all with 20 cycles of ALD Al_2O_3 (buffer layer) on top.

The thickness of the deposited films was measured by ellipsometry (J.A. Woollam M-2000) using a Cauchy model to fit the dielectric layer, and the thickness was also verified by cross-sectional SEM for thick films. XPS was performed on a 45 nm polyimide film (300 cycles) and a 35 nm hybrid film (23 supercycles) with an Escalab 250Xi XPS system (Thermo Scientific) using monochromatic Al Kα X-ray. RBS was measured on a 35 nm hybrid film grown on a flat glassy carbon substrate, using 2 MeV He^+ ion beam at the Institute of Heavy Ion Physics, Peking University. AFM (Bruker, MultiMode 8-HR) was measured in contact mode on a 60 nm polyimide film (400 cycles) and a 35 nm hybrid film grown on flat Si wafer substrates. FTIR spectra were measured with a PerkinElmer Frontier spectrometer on a 45 nm polyimide film and a 35 nm hybrid film grown on KBr plates. UV–vis spectra were measured with a Shimadzu UV-2450 spectrophotometer on a 45 nm polyimide film and a 35 nm hybrid film grown on glass substrates.

DFT calculation

Both DFT and TD-DFT calculations were performed by Gaussian 16 at National Supercomputing Shenzhen Center, using B3LYP functional with 6-311+G(d,p) basis set for geometric optimization and excited states calculation. GD3BJ dispersion correction was included in the calculation[66]. The number of the included excited states was set as 100. Excitations of wavelength larger than 225 nm were used to generate the UV–vis spectra, and Gaussian functions with 0.25 eV in width were used to describe the oscillators. The calculated UV–vis spectra were normalized at the curve maxima (at 239 nm) for better comparison. Multiwfn was used to calculate the transition densities and the spatial distributions of the hole and electron orbitals for the transitions.

Fabrication and characterization of capacitors, TFTs, and circuits

MIM capacitors were fabricated on 20 nm ITO-coated PET substrates. The conductive ITO layer served as the bottom electrode, and the dielectric layer was made of, sequentially, 20 cycles of ALD Al_2O_3 (bottom buffer layer), 30 nm of the polyimide film (200 cycles) or 35 nm of the hybrid film, and 30 cycles of ALD Al_2O_3 (top buffer layer). Then, the top electrodes were made by thermal evaporation of 110 nm Cu through a shadow mask.

TFTs and circuits were fabricated on PEN substrates (Q65HA, Teonex Inc.). Prior to the fabrication, the PEN substrates were sequentially baked at 180 °C for 15 min, oxygen plasma treated at 100 W for 5 min, rinsed sequentially with acetone, ethanol, and deionized water, and then dried under N_2 stream. Top-gate-bottom-contact TFTs were fabricated using SCNT networks as the channels and MCNT networks as the source, drain, and gate electrodes as well as the interconnects in circuits. The bottom S/D electrodes were prepared by spin-coating a layer of MCNT, followed by photolithographic patterning and oxygen plasma etching. The MCNT suspension consisted of 2.0 wt.% MCNT in water (Chinese Academy of Sciences Chengdu Organic Chemistry Co. Ltd.). Then, the channel layer was prepared by spin-coating a layer of SCNT, followed by photolithographic patterning and oxygen plasma etching. The SCNT suspension consisted of 0.02 mg mL^{-1} SCNT, which was prepared by ultrasonicating 1 mg SCNT (NanoIntegris Inc., 99.9%) and 1 mg poly[(m-phenylenevinylene)-co-(2,5-dioctoxy-p-phenylenevinylene)] (PmPV) in 50 mL 1,2-dichloroethane for 6 h. Onto the channel layer was deposited the gate dielectric layer, which consisted 20 cycles of ALD Al_2O_3 (bottom buffer layer), 35 nm of the hybrid film, and 30 cycles of ALD Al_2O_3 (top buffer layer). Then, the gate electrodes and interconnects were prepared on the dielectric layer by spin-coating another MCNT layer followed by photolithographic patterning and oxygen plasma etching. The S/D pads of TFTs were opened by phosphoric acid etching at 70 °C for 2 min with patterned photoresist. The process steps for circuit fabrication are similar to those for TFTs, except that the contact holes were opened prior to the gate electrode preparation. The thickness of the devices and circuits is about 100 nm, excluding the PEN substrate. More fabrication details are illustrated in Supplementary Fig. 14.

The electrical characterizations were mostly performed on a probe station with a semiconductor device analyzer (B1500A, Keysight). Bias was supplied by a signal generator (AFG3101C, Tektronix). The circuit dynamic characteristics were measured with a pulse generator (16440A, Agilent) for input signal generation and an oscilloscope (MSO 2022B, Tektronix) for output signal acquisition. Capacitance was measured by a LCR meter (E4980A, Keysight). Device bending test was conducted on a digitally controlled mechanical stage, as shown in Supplementary Fig. 15.

DATA AVAILABILITY

The data that support the findings of this study are available from the corresponding author upon reasonable request.

CODE AVAILABILITY

The codes used for DFT and TD-DFT calculation, i.e., Gaussian 16, are commercially available. The open-source program used for calculating the transition density of the excitation states, i.e., Multiwfn, can be obtained free of charge from http://sobereva.com/multiwfn/[48].

Received: 4 March 2022; Accepted: 21 June 2022;
Published online: 18 July 2022

REFERENCES

1. Chung, H. U. et al. Skin-interfaced biosensors for advanced wireless physiological monitoring in neonatal and pediatric intensive-care units. *Nat. Med.* **26**, 418–429 (2020).
2. Yetisen, A. K. et al. Wearables in medicine. *Adv. Mater.* **30**, 1706910 (2018).
3. Shim, H. et al. Stretchable elastic synaptic transistors for neurologically integrated soft engineering systems. *Sci. Adv.* **5**, eaax4961 (2019).
4. Molina-Lopez, F. et al. Inkjet-printed stretchable and low voltage synaptic transistor array. *Nat. Commun.* **10**, 2676 (2019).
5. Myny, K. The development of flexible integrated circuits based on thin-film transistors. *Nat. Electron.* **1**, 30–39 (2018).
6. Hu, Y., Peng, L.-M., Xiang, L. & Zhang, H. Flexible integrated circuits based on carbon nanotubes. *Acc. Mater. Res.* **1**, 88–99 (2020).
7. Xiang, L. et al. Recent advances in flexible and stretchable sensing systems: From the perspective of system integration. *ACS Nano* **14**, 6449–6469 (2020).
8. Zhang, H. et al. High-performance carbon nanotube complementary electronics and integrated sensor systems on ultrathin plastic foil. *ACS Nano* **12**, 2773–2779 (2018).
9. Sun, J. et al. Fully R2R-printed carbon-nanotube-based limitless length of flexible active-matrix for electrophoretic display application. *Adv. Electron. Mater.* **6**, 1901431 (2020).
10. Ray, T. R. et al. Bio-integrated wearable systems: A comprehensive review. *Chem. Rev.* **119**, 5461–5533 (2019).
11. Xiang, L., Zhang, H., Hu, Y. & Peng, L.-M. Carbon nanotube-based flexible electronics. *J. Mater. Chem. C* **6**, 7714–7727 (2018).
12. Hirotani, J. & Ohno, Y. Carbon nanotube thin films for high-performance flexible electronics applications. *Top. Curr. Chem.* **377**, 3 (2019).

13. Wang, B.-W. et al. Continuous fabrication of meter-scale single-wall carbon nanotube films and their use in flexible and transparent integrated circuits. *Adv. Mater.* **30**, 1802057 (2018).
14. Sun, D.-M. et al. Mouldable all-carbon integrated circuits. *Nat. Commun.* **4**, 2302 (2013).
15. Lei, T. et al. Low-voltage high-performance flexible digital and analog circuits based on ultrahigh-purity semiconducting carbon nanotubes. *Nat. Commun.* **10**, 2161 (2019).
16. Chen, H., Cao, Y., Zhang, J. & Zhou, C. Large-scale complementary macroelectronics using hybrid integration of carbon nanotubes and IGZO thin-film transistors. *Nat. Commun.* **5**, 4097 (2014).
17. Sun, D.-m et al. Flexible high-performance carbon nanotube integrated circuits. *Nat. Nanotechnol.* **6**, 156–161 (2011).
18. Cao, Q. et al. Medium-scale carbon nanotube thin-film integrated circuits on flexible plastic substrates. *Nature* **454**, 495–500 (2008).
19. Wang, B. et al. High-k gate dielectrics for emerging flexible and stretchable electronics. *Chem. Rev.* **118**, 5690–5754 (2018).
20. Lee, D. et al. Logic circuits composed of flexible carbon nanotube thin-film transistor and ultra-thin polymer gate dielectric. *Sci. Rep.* **6**, 26121 (2016).
21. Wang, Y. et al. Polymer-based gate dielectrics for organic field-effect transistors. *Chem. Mater.* **31**, 2212–2240 (2019).
22. Cai, L. et al. Fully printed stretchable thin-film transistors and integrated logic circuits. *ACS Nano* **10**, 11459–11468 (2016).
23. Lau, P. H. et al. Fully printed, high performance carbon nanotube thin-film transistors on flexible substrates. *Nano Lett.* **13**, 3864–3869 (2013).
24. Lai, H.-C., Pei, Z., Jian, J.-R. & Tzeng, B.-J. Alumina nanoparticle/polymer nanocomposite dielectric for flexible amorphous indium–gallium–zinc oxide thin film transistors on plastic substrate with superior stability. *Appl. Phys. Lett.* **105**, 033510 (2014).
25. Moon, H. et al. Synthesis of ultrathin polymer insulating layers by initiated chemical vapour deposition for low-power soft electronics. *Nat. Mater.* **14**, 628–635 (2015).
26. Kim, M. J. et al. Ultrathin ZrOx-organic hybrid dielectric (EOT 3.2 nm) via initiated chemical vapor deposition for high-performance flexible electronics. *ACS Appl. Mater. Inter.* **11**, 44513–44520 (2019).
27. Choi, J. et al. Heavily crosslinked, high-k ultrathin polymer dielectrics for flexible, low-power organic thin-film transistors (OTFTs). *Adv. Electron. Mater.* **6**, 2000314 (2020).
28. Puurunen, R. L. Surface chemistry of atomic layer deposition: A case study for the trimethylaluminum/water process. *J. Appl. Phys.* **97**, 52 (2005).
29. Putkonen, M., Harjuoja, J., Sajavaara, T. & Niinisto, L. Atomic layer deposition of polyimide thin films. *J. Mater. Chem.* **17**, 664–669 (2007).
30. Sheng, T. et al. Atomic layer deposition of polyimide on microporous polyethersulfone membranes for enhanced and tunable performances. *Aiche J.* **60**, 3614–3622 (2014).
31. Guo, Z. et al. Atomic layer deposition of $FeSe_2$, $CoSe_2$, and $NiSe_2$. *Chem. Mater.* **33**, 2478–2487 (2021).
32. Li, H. et al. Organosulfur precursor for atomic layer deposition of high-quality metal sulfide films. *Chem. Mater.* **32**, 8885–8894 (2020).
33. Zhao, R. et al. Interface energy alignment of atomic-layer-deposited VOx on pentacene: An in situ photoelectron spectroscopy investigation. *ACS Appl. Mater. Inter.* **9**, 1885–1890 (2017).
34. Gao, Y. et al. Efficient charge injection in organic field-effect transistors enabled by low-temperature atomic layer deposition of ultrathin VOx interlayer. *Adv. Funct. Mater* **26**, 4456–4463 (2016).
35. Dupont™, Kapton® Summary of Properties. https://www.dupont.com/electronic-materials/kapton-polyimide-film.html (2021).
36. Zhang, C. et al. Area-selective molecular layer deposition of polyimide on Cu through Cu-catalyzed formation of a crystalline interchain polyimide. *Chem. Mater.* **32**, 5073–5083 (2020).
37. Song, Z. P., Zhan, H. & Zhou, Y. H. Polyimides: Promising energy-storage materials. *Angew. Chem. -Int. Ed.* **49**, 8444–8448 (2010).
38. Snyder, R. W. et al. FTIR Studies of polyimides—Thermal curing. *Macromolecules* **22**, 4166–4172 (1989).
39. Guan, X. H., Chen, G. H. & Shang, C. ATR-FTIR and XPS study on the structure of complexes formed upon the adsorption of simple organic acids on aluminum hydroxide. *J. Environ. Sci.* **19**, 438–443 (2007).
40. Ji, D. Y. et al. Copolymer dielectrics with balanced chain-packing density and surface polarity for high-performance flexible organic electronics. *Nat. Commun.* **9**, 2339 (2018).
41. Tu, N. R. & Kao, K. C. High-field electrical conduction in polyimide films. *J. Appl. Phys.* **85**, 7267–7275 (1999).
42. Kim, M. J. et al. Novel vapor-phase synthesis of flexible, homogeneous organic–inorganic hybrid gate dielectric with sub 5 nm equivalent oxide thickness. *ACS Appl. Mater. Inter.* **10**, 37326–37334 (2018).
43. Lee, B. H., Yoon, B., Anderson, V. R. & George, S. M. Alucone alloys with tunable properties using alucone molecular layer deposition and Al_2O_3 atomic layer deposition. *J. Phys. Chem. C* **116**, 3250–3257 (2012).
44. Brewer, R. T. et al. Ammonia pretreatment for high-kappa dielectric growth on silicon. *Appl. Phys. Lett.* **85**, 3830–3832 (2004).
45. Gong, B. & Parsons, G. N. Quantitative in situ infrared analysis of reactions between trimethylaluminum and polymers during Al_2O_3 atomic layer deposition. *J. Mater. Chem.* **22**, 15672–15682 (2012).
46. Wu, C. et al. Flexible temperature-invariant polymer dielectrics with large bandgap. *Adv. Mater.* **32**, 2000499 (2020).
47. Ma, Y. P. et al. Structure effect on transition mechanism of UV-visible absorption spectrum in polyimides: A density functional theory study. *Polymer* **148**, 356–369 (2018).
48. Lu, T. & Chen, F. W. Multiwfn: A multifunctional wavefunction analyzer. *J. Comput. Chem.* **33**, 580–592 (2012).
49. Liu, Z. Y., Lu, T. & Chen, Q. X. An sp-hybridized all-carboatomic ring, cyclo 18 carbon: Electronic structure, electronic spectrum, and optical nonlinearity. *Carbon* **165**, 461–467 (2020).
50. Li, H., Guo, Z. & Wang, X. Atomic-layer-deposited ultrathin Co9S8 on carbon nanotubes: an efficient bifunctional electrocatalyst for oxygen evolution/reduction reactions and rechargeable Zn–air batteries. *J. Mater. Chem. A* **5**, 21353–21361 (2017).
51. Xiong, W. et al. Rational bottom-up engineering of electrocatalysts by atomic layer deposition: A case study of $Fe_xCo_{1-x}Sy$-based catalysts for electrochemical hydrogen evolution. *ACS Energy Lett.* **2**, 2778–2785 (2017).
52. Tang, J. et al. Flexible CMOS integrated circuits based on carbon nanotubes with sub-10 ns stage delays. *Nat. Electron.* **1**, 191–196 (2018).
53. Chortos, A. et al. Mechanically durable and highly stretchable transistors employing carbon nanotube semiconductor and electrodes. *Adv. Mater.* **28**, 4441–4448 (2016).
54. Zhao, Y. et al. Three-dimensional flexible complementary metal-oxide-semiconductor logic circuits based on two-layer stacks of single-walled carbon nanotube networks. *ACS Nano* **10**, 2193–2202 (2016).
55. Xiang, L. et al. Low-power carbon nanotube-based integrated circuits that can be transferred to biological surfaces. *Nat. Electron.* **1**, 237–245 (2018).
56. Yu, W. J. et al. Small hysteresis nanocarbon-based integrated circuits on flexible and transparent plastic substrate. *Nano Lett.* **11**, 1344–1350 (2011).
57. Honda, W. et al. High-performance, mechanically flexible, and vertically integrated 3D carbon nanotube and InGaZnO complementary circuits with a temperature sensor. *Adv. Mater.* **27**, 4674–4680 (2015).
58. Nishio, Y. et al. Low-voltage operable and strain-insensitive stretchable all-carbon nanotube integrated circuits with local strain suppression layer. *Adv. Electron. Mater.* **7**, 2000674 (2021).
59. Wei, M. et al. Air-stable N-type printed carbon nanotube thin film transistors for CMOS logic circuits. *Carbon* **163**, 145–153 (2020).
60. Zhang, X. et al. Flexible CMOS-like circuits based on printed P-type and N-type carbon nanotube thin-film transistors. *Small* **12**, 5066–5073 (2016).
61. Luo, M. et al. Radiation-hard and repairable complementary metal–oxide–semiconductor circuits integrating n-type indium oxide and p-type carbon nanotube field-effect transistors. *ACS Appl. Mater. Inter.* **12**, 49963–49970 (2020).
62. Yang, R. et al. Semiconductor-based dynamic heterojunctions as an emerging strategy for high direct-current mechanical energy harvesting. *Nano Energy* **83**, 105849 (2021).
63. Chung, H. U. et al. Binodal, wireless epidermal electronic systems with in-sensor analytics for neonatal intensive care. *Science* **363**, eaau0780 (2019).
64. Guo, Z. et al. Low-temperature atomic layer deposition of high purity, smooth, low resistivity copper films by using amidinate precursor and hydrogen plasma. *Chem. Mater.* **27**, 5988–5996 (2015).
65. Li, H. et al. Vapor-phase atomic layer deposition of nickel sulfide and its application for efficient oxygen-evolution electrocatalysis. *Chem. Mater.* **28**, 1155–1164 (2016).
66. Grimme, S., Ehrlich, S. & Goerigk, L. Effect of the damping function in dispersion corrected density functional theory. *Comput. Chem.* **32**, 1456–1465 (2011).

ACKNOWLEDGEMENTS

This work is financially supported by National Natural Science Foundation of China (62074008, 22175005 and 51961165105), Guangdong Basic and Applied Basic Research Foundation (2020B1515120039), and Shenzhen Fundamental Research Program (GXWD20201231165807007-20200827122756001, JCYJ20180507181702150, JCYJ20200109110628172, and GXWD20201231165807007-20200802205241003). RBS measurements were supported by State Key Laboratory of Nuclear Physics and Technology, Peking University under contract no. NPT2020KFJ20.

AUTHOR CONTRIBUTIONS

M.Z. and X.W. conceived, provided methods, and supervised the project. Q.H. and J.W. fabricated and characterized devices. J.W. performed material characterizations. Q.H. and C.L. designed and analyzed circuits. J.W. and J.Z. performed DFT calculations. Q.H., C.L., W.W., Y.H., and Y.Z. performed electrical characterizations. Q.H., J.W., M.Z., X.W., H.J., S.Z., and H.M. discussed the results. Q.H., J.W., M.Z., and X.W. wrote the manuscript.

COMPETING INTERESTS

The authors declare no competing interests.

ADDITIONAL INFORMATION

Supplementary information The online version contains supplementary material available at https://doi.org/10.1038/s41528-022-00190-8.

Correspondence and requests for materials should be addressed to Min Zhang or Xinwei Wang.